The James Clerk Maxwell Telescope Nearby Galaxies Legacy Survey – IX. ^{12}CO $J = 3{\rightarrow}2$ observations of NGC 2976 and NGC 3351

Boon-Kok Tan,[1,2]★ J. Leech,[1] D. Rigopoulou,[1,3] B. E. Warren,[4,5] C. D. Wilson,[4]
D. Attewell,[4] M. Azimlu,[6] G. J. Bendo,[7] H. M. Butner,[8] E. Brinks,[9] P. Chanial,[10]
D. L. Clements,[10] V. Heesen,[9, 11] F. Israel,[12] J. H. Knapen,[13,14] H. E. Matthews,[15]
A. M. J. Mortier,[10] S. Mühle,[16] J. R. Sánchez-Gallego,[13,17] R. P. J. Tilanus,[18,19]
A. Usero,[8,20] P. van der Werf[12] and M. Zhu[21]

[1]*Department of Astrophysics, University of Oxford, Keble Road, Oxford OX1 3RH, UK*
[2]*Institute for Research and Innovation, Wawasan Open University, 54 Jalan Sultan Ahmad Shah, 10050 Penang, Malaysia*
[3]*Rutherford Appleton Laboratory, Chilton, Didcot OX11 0QX, UK*
[4]*Department of Physics & Astronomy, McMaster University, Hamilton, Ontario L8S 4M1, Canada*
[5]*Intl. Centre for Radio Astronomy Research, M468, University of Western Australia, 35 Stirling Hwy, Crawley, WA 6009, Australia*
[6]*Harvard–Smithsonian Center for Astrophysics, 60 Garden St., Cambridge, MA 02138, USA*
[7]*UK ALMA Regional Centre Node, Jodrell Bank Centre for Astrophysics, University of Manchester, Oxford Rd., Manchester M13 9PL, UK*
[8]*Department of Physics and Astronomy, James Madison University, MSC 4502-901 Carrier Drive, Harrisonburg, VA 22807, USA*
[9]*Centre for Astrophysics Research, University of Hertfordshire, College Lane, Hatfield AL10 9AB, UK*
[10]*Astrophysics Group, Imperial College London, Blackett Laboratory, Prince Consort Road, London SW7 2AZ, UK*
[11]*School of Physics and Astronomy, University of Southampton, Southampton SO17 1BJ, UK*
[12]*Sterrewacht Leiden, Leiden University, PO Box 9513, NL-2300 RA Leiden, the Netherlands*
[13]*Instituto de Astrofísica de Canarias, E-38200 La Laguna, Spain*
[14]*Departamento de Astrofísica, Universidad de La Laguna, E-38200 La Laguna, Tenerife, Spain*
[15]*NRC, Herzberg Institute of Astrophysics, DRAO, PO Box 248, White Lake Road, Penticton, British Columbia V2A 69J, Canada*
[16]*Argelander-Institut für Astronomie, Universität Bonn, Auf dem Hügel 71, D-53121 Bonn, Germany*
[17]*Department of Physics & Astronomy, University of Kentucky, Lexington, KY 40506-0055, USA*
[18]*Joint Astronomy Centre, 660 N. A'ohoku Pl., Hilo, HI 96720, USA*
[19]*Netherlands Organisation for Scientific Research, PO Box 93138, NL-2509 AC The Hague, the Netherlands*
[20]*Observatorio Astronómico Nacional, C. Alfonso XII 3, E-28014 Madrid, Spain*
[21]*National Astronomical Observatories, Chinese Academy of Science, 20A Datun Road, Chaoyang District, Beijing 100012, China*

ABSTRACT

We present ^{12}CO $J = 3{\rightarrow}2$ maps of NGC 2976 and NGC 3351 obtained with the James Clerk Maxwell Telescope (JCMT), both early targets of the JCMT Nearby Galaxy Legacy Survey (NGLS). We combine the present observations with ^{12}CO $J = 1{\rightarrow}0$ data and find that the computed ^{12}CO $J = 3{\rightarrow}2$ to ^{12}CO $J = 1{\rightarrow}0$ line ratio (R_{31}) agrees with values measured in other NGLS field galaxies. We compute the M_{H_2} value and find that it is robust against the value of R_{31} used. Using H$_I$ data from The H$_I$ Nearby Galaxy Survey, we find a tight correlation between the surface density of H$_2$ and star formation rate density for NGC 3351 when ^{12}CO $J = 3{\rightarrow}2$ data are used. Finally, we compare the ^{12}CO $J = 3{\rightarrow}2$ intensity with the polycyclic aromatic hydrocarbon (PAH) 8 µm surface brightness and find a good correlation in the high surface brightness regions. We extend this study to include all 25 *Spitzer* Infrared Nearby Galaxies Survey galaxies within the NGLS sample and find a tight correlation at large spatial scales. We suggest that both PAH 8 µm and ^{12}CO $J = 3{\rightarrow}2$ are likely to originate in regions of active star formation.

Key words: ISM: molecules – galaxies: individual: NGC 2976 – galaxies: individual: NGC 3351 – galaxies: ISM – infrared: galaxies.

★ E-mail: tanbk@astro.ox.ac.uk

1 INTRODUCTION

Observations of molecular gas are essential for understanding the role of star formation in the evolution of galaxies. Because direct detection of molecular hydrogen (H_2) is difficult, carbon monoxide (CO) is used as its proxy. Many extragalactic surveys of low-J rotational transitions of CO have been conducted so far (e.g. Braine et al. 1993; Sage 1993; Young et al. 1995; Elfhag et al. 1996; Meier et al. 2001; Albrecht et al. 2004; Israel 2005), the majority being single pointing observations that do not provide any information on the spatial distribution of the emission. High angular resolution interferometric surveys have also been conducted (e.g. Sakamoto et al. 1999; Regan et al. 2001; Helfer et al. 2003), but most of them have targeted the central regions of the galaxies due to the limited field size. High-sensitivity multipixel array receivers (on single-dish telescopes) are now providing much faster speeds for mapping interesting structures in the interstellar medium (ISM) across entire galactic discs. Two surveys using this type of focal plane array receivers were recently carried out, one by Leroy et al. (2009) using Heterodyne Receiver Array (HERA) on the Institut de Radio Astronomie Millimétrique 30 m telescope to map $^{12}CO\ J = 2{\rightarrow}1$ and another by Kuno et al. (2007) using the Beam Array Receiver System on Nobeyama Radio Observatory (NRO) to map $^{12}CO\ J = 1{\rightarrow}0$, in nearby galaxies.

The Nearby Galaxy Legacy Survey (NGLS; Wilson et al. 2009, 2012) uses the James Clerk Maxwell Telescope (JCMT) to map $^{12}CO\ J = 3{\rightarrow}2$ emission from nearby galaxies. The $^{12}CO\ J = 3{\rightarrow}2$ transition traces the warmer and denser regions of the molecular gas that are more directly related to star-forming regions (Wilson et al. 2009, and references therein). The entire JCMT NGLS sample consists of 155 nearby galaxies, each with spectral line observations at 345 GHz, made with the Heterodyne Array Receiver Program for *B*-band (HARP-B) receiver (Smith et al. 2003). The details of the NGLS can be found in Wilson et al. (2012).

NGC 2976 and NGC 3351 were observed during the early stages of the NGLS. NGC 2976 is a dwarf galaxy on the outskirts of the M81 group, in weak tidal interaction with the group (Appleton, Davies & Stephenson 1981; Yun 1999). Although the galaxy contains primarily an older stellar population, there are indications (Williams et al. 2010) that there are sites of intense star formation at the two bright regions near the north and south ends of the galaxy's major axis (Dale et al. 2009). NGC 3351 is a starburst galaxy with ring structures (Colina et al. 1997; Elmegreen et al. 1997; Knapen, Pérez-Ramírez & Laine 2002; Swartz et al. 2006; Hägele et al. 2007; Comerón et al. 2013) that displays a very young starburst population. It is thus interesting to understand the effect of such different environments on the physical conditions of the molecular component of the ISM within these two galaxies. Using the improved spatial resolution of the NGLS $^{12}CO\ J = 3{\rightarrow}2$ survey, we can resolve the sites of *warmer*, *denser* molecular hydrogen, and investigate the correlation of this observable with other components of the ISM observed in different wavebands.

Another important motivation for the NGLS is to probe the interplay between dust and gas in nearby galaxies. Polycyclic aromatic hydrocarbons (PAHs) have often been used as an indicator of star formation activity in external galaxies (Zhu et al. 2008; Kennicutt et al. 2009). An alternative theory that PAH emission is not related to star formation but instead is associated with continuum emission from cold dust has also been proposed by Haas, Klaas & Bianchi (2002). However, results from the *Spitzer* Infrared Nearby Galaxies Survey (SINGS), a comprehensive infrared imaging and spectroscopic survey of 75 nearby galaxies using the *Spitzer Space Telescope* (hereafter *Spitzer*), indicated that the relation between PAHs and star formation extends to spatial scales beyond 1 kpc, although the relation breaks down on smaller spatial scales (Calzetti et al. 2005, 2007; Bendo et al. 2006, 2008; Prescott et al. 2007; Zhu et al. 2008; Kennicutt et al. 2009; Calzetti 2012).

In this paper, we report the $^{12}CO\ J = 3{\rightarrow}2$ measurements of NGC 2976 and NGC 3351. We describe the basic properties of the two galaxies in Section 2. The details of the observations and data reduction are presented in Section 3. We present our results and discussion in Section 4 where we calculate $^{12}CO\ J = 3{\rightarrow}2$ to $^{12}CO\ J = 1{\rightarrow}0$ line ratios, derive the molecular gas masses and study the correlation between the $^{12}CO\ J = 3{\rightarrow}2$ line emission and emission from PAHs. Finally, we summarize our conclusions in Section 5.

2 TARGET GALAXIES

NGC 2976 is an SAB(s:)d peculiar dwarf disc galaxy (Buta, in preparation) in the M81 group. Single-beam $^{12}CO\ J = 3{\rightarrow}2$ and $^{12}CO\ J = 2{\rightarrow}1$ observations have been presented by Israel (2005), while $^{12}CO\ J = 1{\rightarrow}0$ emission has been mapped at high resolution by Simon et al. (2003) using the Berkeley–Illinois–Maryland Association (BIMA) interferometer. These observations, however, only partially covered the two bright end regions. The present NGLS $^{12}CO\ J = 3{\rightarrow}2$ map covers a rectangular area corresponding to $D_{25}/2$, and is therefore wide enough to include both bright complexes.

NGC 3351 is an (R')SB(r,nr)a spiral galaxy (Buta, in preparation) displaying high-mass star formation in a 15.3 arcsec × 11.2 arcsec circumnuclear ring (hereafter the 15 arcsec ring; Alloin & Nieto 1982; Buta & Crocker 1993; Colina et al. 1997; Elmegreen et al. 1997; Comerón et al. 2010, 2013), fuelled by gas accreted through a stellar bar (Swartz et al. 2006). Most of the NGC 3351 studies have so far focused on this bright central region of the galaxy. However, the optical image (Frei et al. 1996; Abazajian et al. 2009) shown in Fig. 2(a) shows a faint ring of ∼ 2 arcmin diameter (hereafter the 2 arcmin ring) encircling the bar, with signs of spiral arms extending from this ring towards the outermost pseudo-ring feature (major axis diameter ∼ 5.5 arcmin, minor axis ∼ 3.6 arcmin; Buta & Crocker 1993). These features are within the area covered by our $^{12}CO\ J = 3{\rightarrow}2$ map of NGC 3351 presented in this paper.

The general properties of NGC 2976 and NGC 3351 taken from de Vaucouleurs et al. (1995) (unless otherwise stated) are summarized in Table 1.

Table 1. General properties of NGC 2976 and NGC 3351 taken from the literature.

General properties	NGC 2976	NGC 3351
Type	SAB(s:)d pec	(R')SB(r,nr)a
RA (J2000)	09:47:15.6	10:43:58.0
Dec. (J2000)	+67:54:50	+11:42:15
Distance (Mpc)[a]	3.56	9.33
Incl. angle[b]	54°	39°
$D_{25}/2$ (arcmin)[c]	2.9 × 1.5	3.8 × 2.2

[a]Reference for the distance to NGC 2976 from Karachentsev et al. (2002) and for NGC 3351 from Freedman et al. (2001).
[b]Inclination angle from de Blok et al. (2008).
[c]From Buta, Corwin & Odewahn (2007).

2.1 Archival data

Both NGC 2976 and NGC 3351 are part of the SINGS (Kennicutt et al. 2003) and have rich multiwavelength ancillary data available. Although a number of ^{12}CO data sets at various transitions are available, most of these are single-beam data and thus the comparison with our ^{12}CO $J = 3→2$ maps is challenging. Furthermore, the spatial distribution information in our high-resolution ^{12}CO $J = 3→2$ map will also be under-utilized if used together with these single-beam data. Hence, in this paper, we shall discard the use of single-beam data from the literature, but focus only on the available ^{12}CO $J = 1→0$ maps. For NGC 3351, ^{12}CO $J = 1→0$ maps are available from the single-dish NRO (Kuno et al. 2007)[1] and the BIMA Survey of Nearby Galaxies (SONG; Helfer et al. 2003). We used ^{12}CO $J = 1→0$ maps from NRO as their beam size (15 arcsec) closely matches the ^{12}CO $J = 3→2$ beam size of HARP-B on the JCMT. Unfortunately, NGC 2976 was not included in the NRO survey. Hence, the ^{12}CO $J = 1→0$ map for NGC 2976 was retrieved from the BIMA SONG survey.[2] However, we have not used this map for any further analysis, but have only displayed the ^{12}CO $J = 1→0$ distribution within the galaxy in Fig. 1, as the BIMA ^{12}CO $J = 1→0$ map for NGC 2976 has poor *uv*-plane sampling.

The *Spitzer* Infrared Array Camera (IRAC) 3.6 and 8 µm data and Multiband Imaging Photometer for *Spitzer* (MIPS) 24 µm data used in this study were downloaded from the SINGS website.[3] The optical images for both galaxies were retrieved from the seventh data release of the Sloan Digital Sky Survey (SDSS).[4] The H I images were downloaded from the The H I Nearby Galaxy Survey (THINGS)[5] and the far-ultraviolet (FUV) images used to produce the star formation rate (SFR) surface density images, in conjunction with the 24 µm data, were retrieved from the *Galaxy Evolution Explorer* (*GALEX*) data release.[6]

3 OBSERVATIONS AND DATA REDUCTION

The ^{12}CO $J = 3→2$ (rest frequency 345.796 GHz) observations for NGC 2976 were carried out over two nights between 2007 November and 2008 January, while observations for NGC 3351 took place over two runs in 2008 January. The instrument used was HARP-B which has 16 superconductor–insulator–superconductor heterodyne mixers arranged in a 4 × 4 array with 30 arcsec row and column separation. This corresponds to a 2 arcmin square footprint on the sky. HARP-B operates over a frequency range of 325–375 GHz and the average full width at half-maximum (FWHM) beam width is 14.5 arcsec. The receiver operates with the Auto-Correlation Spectrometer and Imaging System (ACSIS; Buckle et al. 2009) as the back-end data processing unit. The observations for both galaxies in this paper were made using a 1 GHz ACSIS bandwidth with a spectral resolution of 0.488 MHz. The main-beam efficiencies (η_{MB}) used to convert the corrected antenna temperature (T_A^*) to the main-beam brightness temperature (T_{mb}) were determined from observations of bright planets. All data presented in this paper were calibrated to the T_{mb} scale using $\eta_{MB} = 0.6$.

Both NGC 2976 and NGC 3351 were raster scanned using a basket-weave technique with half-array steps [58.2 arcsec, the

reader is referred to the appendix in Warren et al. (2010) for a more detailed description of the steps used in the data reduction process]. This ensured that all of the area within the target scan region, defined to include all of the optical galactic emission, was fully sampled. These fully sampled maps were made repeatedly until the target root-mean-square noise of the combined scans (less than 19 mK in T_A^* scale) was achieved within a frequency bin of 20 km s^{-1} resolution. The observational details for each galaxy are summarized in Table 2.

3.1 Data reduction

The spectral data reduction and analysis was done mainly using the *Starlink*[7] software packages (Jenness et al. 2009). We used Kernel Application Package (KAPPA)[8] and Sub-Millimetre User Reduction Facility applications within *Starlink* as the main reduction tools. Graphical Astronomy and Image Analysis Tool and Spectrum Analysis Tool were used for analysis and visualization purposes. Data collected under the NGLS were processed primarily following the steps outlined in Warren et al. (2010), with some modifications depending on the characteristics of the individual galaxy and the quality of the observed data (Wilson et al. 2012).

3.1.1 R_{31} line ratio

To derive the R_{31} map for NGC 3351 using the NRO's ^{12}CO $J = 1→0$ map, we re-gridded the ^{12}CO $J = 1→0$ map to match our pixel size (7.28 arcsec) and calculated the R_{31} ratio map by performing a pixel-by-pixel division of the resulting ^{12}CO $J = 3→2$ and ^{12}CO $J = 1→0$ maps. We did not convolve and match the beam of both maps because the beam sizes of NRO (15 arcsec) and HARP-B (14.5 arcsec) are very similar. As explained in Section 2.1, the BIMA ^{12}CO $J = 1→0$ map for NGC 2976 has poor *uv*-plane sampling; hence, we have not produced the R_{31} map for NGC 2976.

3.1.2 8 µm data and radial profile

The point spread function (PSF) of *Spitzer* images is highly non-Gaussian. We thus created convolution kernels, following recipes from Gordon et al. (2008) and Bendo et al. (2010), to match the PSFs to those of HARP-B. These kernels were created, for each waveband, using STINYTIM[9] (Krist 2002), and convolved with the *Spitzer* images to match the HARP-B beam. We used the KAPPA routine `convolve` for this task. Further details of the PSF matching for HARP-B and *Spitzer* images can be found in Bendo et al. (2010).

The originally reduced IRAC 8 µm data from the SINGS sampled emission from both stars and dust. To produce an 8 µm image with surface brightness due to dust only (hereinafter dust-only 8 µm image), we needed to remove the stellar contribution using the 3.6 µm image (Helou et al. 2004; Smith et al. 2007) following the steps outlined in Bendo et al. (2010). First, we determined and subtracted the residual background of both the 3.6 and 8 µm images by fitting a smoothed gradient of the background brightness outside the galaxy disc. Regions with 3.6–8 µm surface brightness ratio ≥5 were masked out as bright foreground stars. The effective aperture corrections were then applied to both images by

[1] http://www.nro.nao.ac.jp/~nro45mrt/COatlas/

[2] http://nedwww.ipac.caltech.edu/level5/March02/SONG/SONG.html

[3] http://sings.stsci.edu/

[4] http://www.sdss.org/

[5] http://www.mpia.de/THINGS/Data.html

[6] http://galex.stsci.edu/GR4/

[7] *Starlink* is maintained by the Joint Astronomy Centre (JAC) (http://www.starlink.ac.uk).

[8] http://docs.jach.hawaii.edu/star/sun95.htx/sun95.html

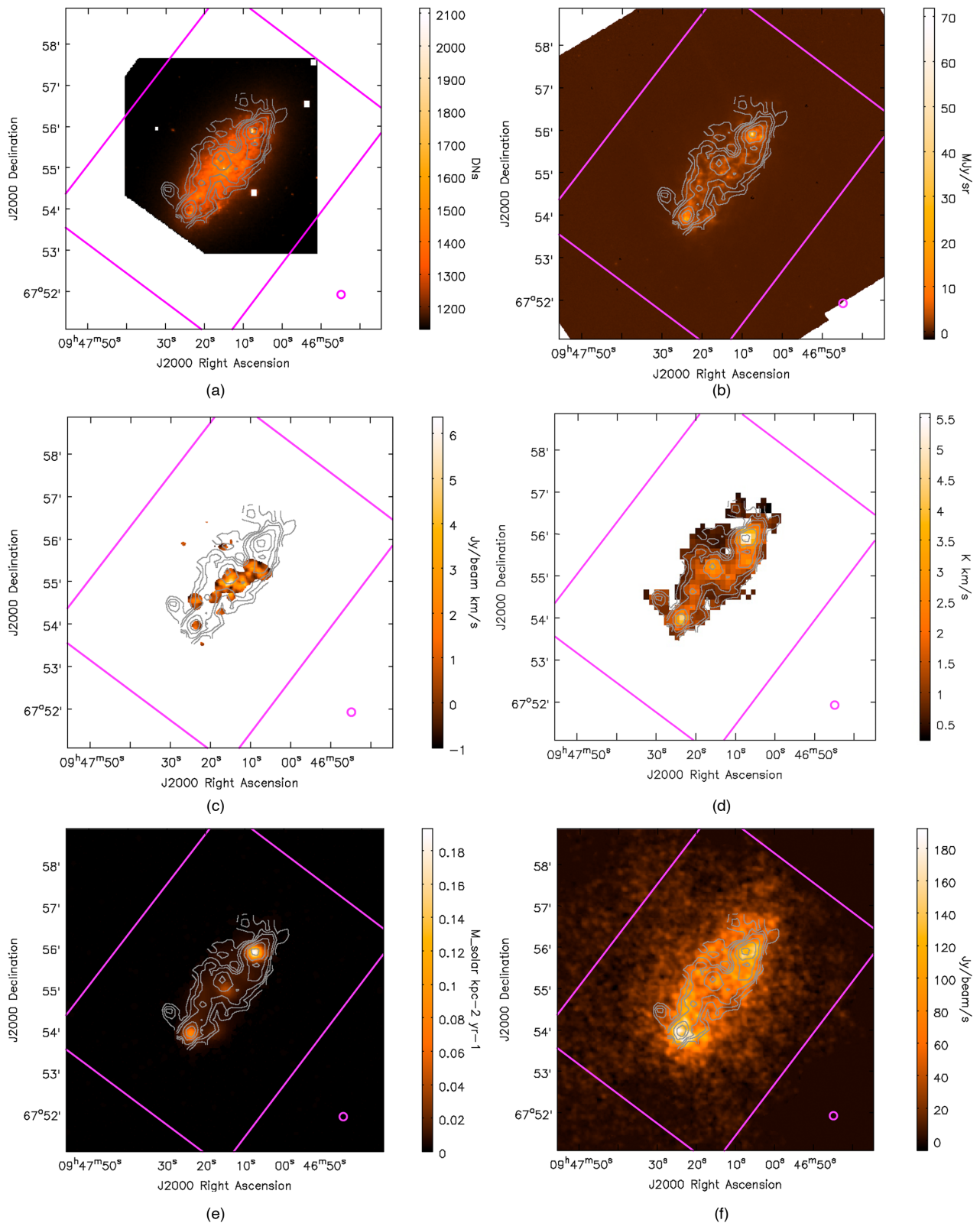[9] http://ssc.spitzer.caltech.edu/archanaly/contributed/browse.html

Figure 1. Contours of the ^{12}CO $J = 3\rightarrow2$ data of NGC 2976 overlaid on the corresponding ancillary images from the archives. The contour levels are 0.36 (3σ), 0.72, 1.08, 2.0, 3.0 and 5.0 K km s^{-1} (temperature in T_{mb}). In all panels, a magenta box is drawn to show the region mapped by HARP-B, and a magenta circle to indicate the 14.5 arcsec angular resolution of the ^{12}CO $J = 3\rightarrow2$ data. All images are oriented north up and east to the left. The image representing Σ_{SFR} has been convolved to the HARP-B beam size. The native resolution of each map is listed along with the title of each individual panels. (a) Optical (SDSS, 1.35 arcsec). (b) 8 μm (*Spitzer* IRAC, 0.75 arcsec). (c) ^{12}CO $J = 1\rightarrow0$ (BIMA, 1 arcsec). (d) ^{12}CO $J = 3\rightarrow2$ (JCMT NGLS, 7.27 arcsec). (e) Σ_{SFR} (*Spitzer* MIPS 24 μm and *GALEX* FUV, 1.5 arcsec). (f) H I (THINGS, 1.5 arcsec).

Table 2. Observation dates and set-up used in the observing runs for NGC 2976 and NGC 3351.

Parameters	NGC 2976	NGC 3351
Observing dates	2007 November 25	2008 January 07
	2008 January 06	2008 January 12
Pos. angle (major axis)	143°	13°
Height of map	294 arcsec	348 arcsec
Width of map	210 arcsec	252 arcsec
T_{sys}	341 K	409 K
ΔT_A^*	13.3 mK	16.2 mK
Pixel size	7.2761 arcsec	7.2761 arcsec

multiplying the correction factors, 0.944 for the 3.6 μm image and 0.737 for the 8 μm image, respectively, following the calibration recommendation in Reach et al. (2005). Finally, we subtracted the stellar continuum (represented by the final 3.6 μm image) from the 8 μm surface brightness images (Helou et al. 2004) using

$$I_{8\,\mu m}^{dust-only} = I_{8\,\mu m}^{raw} - 0.232 I_{3.6\,\mu m}^{raw}, \quad (1)$$

where $I_{8\,\mu m}^{raw}$ and $I_{3.6\,\mu m}^{raw}$ are the raw 8 and 3.6 μm intensity map from the IRAC pipeline, and $I_{8\,\mu m}^{dust-only}$ is the final dust-only 8 μm intensity map. Note that the IRAC 8 μm image of NGC 3351 was affected by the muxbleed artefact (Laine 2011), so this area has been masked out.

To create a radial profile, we binned the corresponding maps into a number of elliptical annuli. The ellipticity of the annulus was defined by the ratio of the galaxy's major and minor axis lengths. The width of the annulus was about 14.5 arcsec for ^{12}CO $J = 3\rightarrow2$ data and 5.25 arcsec for PAH 8 μm data, defined along the major axis of the galaxy. The radial surface brightness was then the average of the brightness within each ellipse.

3.1.3 SFR surface density

For the SFR surface density maps, we combined the *GALEX* FUV data with the *Spitzer* 24 μm maps. The FUV samples the photospheric emission from the O and B stars which relates to the unobscured star formation, whereas the 24 μm flux traces the emission from dust emission heated by the young stars embedded within. We estimated the SFR surface density using

$$\Sigma_{SFR} = 8.1 \times 10^{-2} I_{FUV} + 3.2 \times 10^{-3} I_{24}, \quad (2)$$

from Leroy et al. (2008), where Σ_{SFR} is the estimated SFR surface density having units of $M_\odot$ kpc^{-2} yr^{-1} and both FUV and 24 μm intensity are in MJy sr^{-1}. We refer the reader to the appendix of Leroy et al. (2008) for details on the calibration steps.

4 RESULTS AND DISCUSSION

In Figs 1 and 2, we show the reduced ^{12}CO $J = 3\rightarrow2$ maps of NGC 2976 and NGC 3351, respectively, together with the ancillary maps of ^{12}CO $J = 1\rightarrow0$, IRAC 8 μm, optical image from SDSS, H I image from THINGS and SFR surface density map. All maps shown are in their native resolution (except the Σ_{SFR} map that was convolved to the HARP-B beam size), overlaid with the contours of our NGLS ^{12}CO $J = 3\rightarrow2$ data.

The NGC 2976 ^{12}CO $J = 3\rightarrow2$ map traces an inverse-S-like feature along the major axis. The structure is not seen in the other wavebands discussed here but does exist in the ^{12}CO $J = 2\rightarrow1$ image from the HERA CO-Line Extragalactic Survey (HERACLES;

Leroy et al. 2009). This is possibly caused by the lower resolution of the CO maps compared to images at other wavebands. This results in small-scale structures being smoothed out in the CO map, hence, making the large structure easier to identify. In both the ^{12}CO $J = 2\rightarrow1$ and our ^{12}CO $J = 3\rightarrow2$ maps, the emission near the two ends of the major axis is stronger in comparison to the central region. The same strong emission is detected in the IRAC 8 μm, MIPS 24 μm and THINGS H I observations but not in the optical images.

A weak detection near the central region of our ^{12}CO $J = 3\rightarrow2$ map is only evident in the SFR surface density image, indicating the existence of hot dust in this region. We note the presence of a faint blob near the centre of this map although it appears to be slightly shifted compared to the ^{12}CO $J = 3\rightarrow2$ detection. This central region of emission is detected in ^{12}CO $J = 1\rightarrow0$ from the BIMA SONG observations, and the position is closer to the MIPS 24 μm central detection location. Due to the small area covered by of the BIMA footprint, the north-west bright end region was partly missed, and only the south-east bright end was detected.

The ^{12}CO $J = 3\rightarrow2$ line width of the south-east bright end in NGC 2976 is narrower, with half-power line width of around 15 km s^{-1}, compared to the north-west bright end of around 30 km s^{-1}. The spectra of these two bright end regions are shown in Figs 3(a) and (b). The peak intensity in T_{MB} is 0.14 K. The emission line can be traced along the inverse-S-like structure from the south-east end towards the north-west end, with the central velocity of the line shifting from −53 towards 68 km s^{-1}. The reader is referred to Wilson et al. (2012) for the velocity field (moment 1) and the velocity dispersion (moment 2) maps of the galaxy.

NGC 3351 has a dominant circumnuclear region detected in all wavebands. The distribution of the ^{12}CO $J = 3\rightarrow2$ integrated intensity across the galactic region displays a huge contrast between the dominant centre and the surrounding area. Only a fraction of the area around the southern part of the 2 arcmin ring is detected in our ^{12}CO $J = 3\rightarrow2$ map. The signal from the northern part of the ring is weak and therefore we do not trace the entire ring structure. The bar that is visible in the optical image is not traced in our ^{12}CO $J = 3\rightarrow2$ map either.

The complex structure to the south-west of the nucleus, between the centre of the galaxy and the 2 arcmin ring, only shows up in our ^{12}CO $J = 3\rightarrow2$ map. The structure extending from the nucleus towards the southern ring on the east also seems to be offset from the detection region in the NRO ^{12}CO $J = 1\rightarrow0$ map. However, this south-east complex and the branch extending slightly towards the north-west are in fact tracing the dust lane (Swartz et al. 2006) surrounding the nuclear region. These dust lanes are visible in the single-filter optical image,[10] and they extend along the leading edge of a bar that is oriented at an angle of 110° east of north. From the IRAC 3.6 μm and the optical image, this bar terminates at the 2 arcmin ring, with faint spiral arms extending beyond the ring. As well as the double ring structure (see Section 2), NGC 3351 has an interesting double bar feature, too. An inner bar terminating at the 15 arcsec ring is detected in the BIMA ^{12}CO $J = 1\rightarrow0$ observation (Helfer et al. 2003). This 15 arcsec bar is almost perpendicular to the outer 2 arcmin bar, but is too small to be resolved at the resolution of HARP-B.

The ^{12}CO $J = 3\rightarrow2$ emission line near the central region of NGC 3351 exhibits a prominent twin peak feature, as depicted in Fig. 3(c). This feature points to the rotation of the 15 arcsec ring
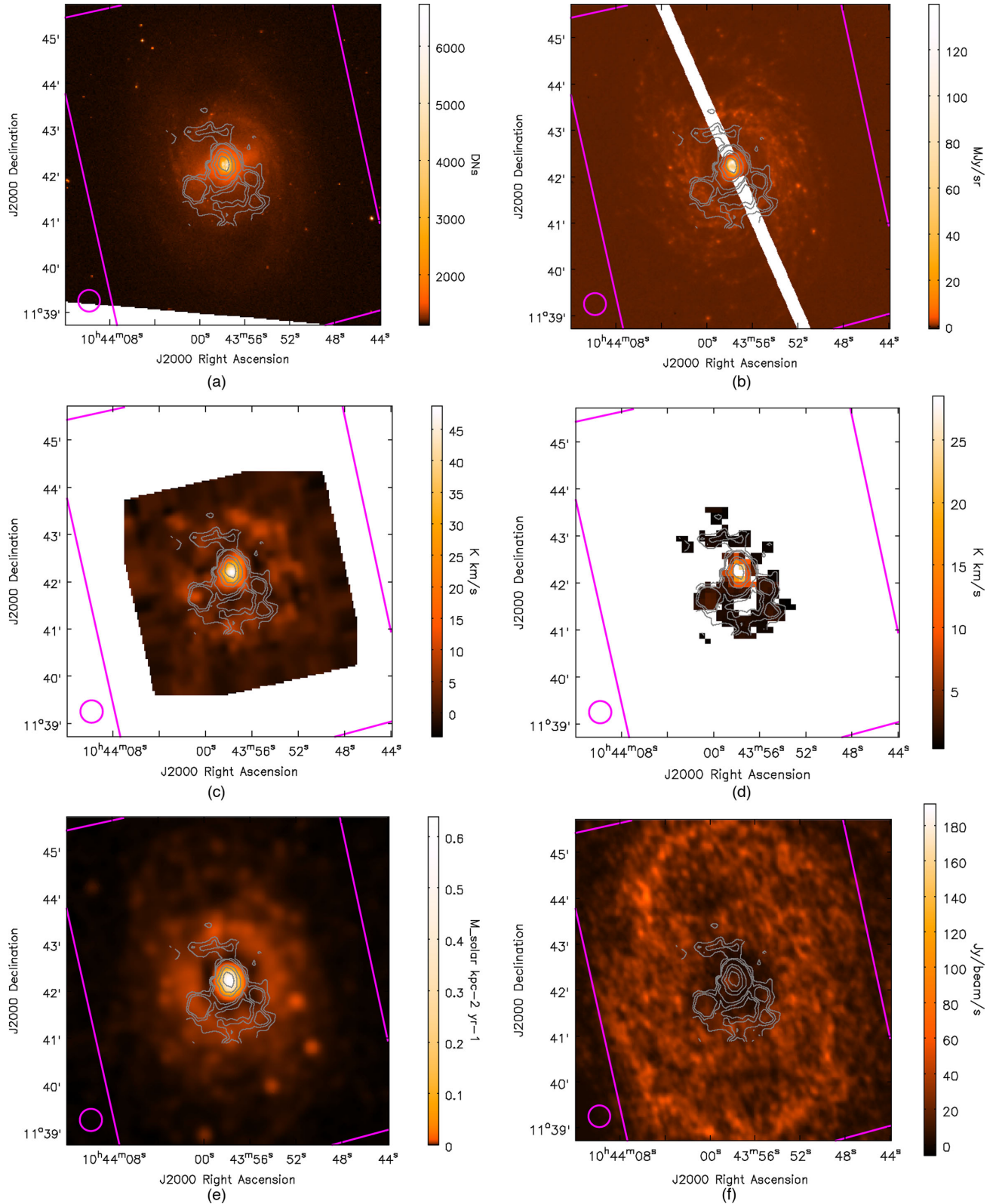
---

[10] Refer to fig. 1 in Swartz et al. (2006).

Figure 2. Contours of the ^{12}CO $J = 3 \rightarrow 2$ data of NGC 3351 overlaid on the corresponding ancillary images from the archives. The contour levels are 0.43 (3σ), 0.86, 1.29, 5.0, 10.0, 20.0 and 30.0 K km s^{-1} (temperature in T_{mb}). In all panels, a magenta box is drawn to show the region mapped by HARP-B, and a magenta circle to indicate the 14.5 arcsec angular resolution of the ^{12}CO $J = 3 \rightarrow 2$ data. All images are oriented north up and east to the left. The 8 μm image is affected by muxbleed (Laine 2011); hence, the affected area is blanked out. The image representing Σ_{SFR} has been convolved to the HARP-B beam size. The native resolution of each map is listed along with the title of each individual panels. (a) Optical (SDSS, 1.35 arcsec). (b) 8 μm (*Spitzer* IRAC, 0.75 arcsec). (c) ^{12}CO $J = 1 \rightarrow 0$ (NRO, 1 arcsec). (d) ^{12}CO $J = 3 \rightarrow 2$ (JCMT NGLS, 7.27 arcsec). (e) Σ_{SFR} (*Spitzer* MIPS 24 μm and *GALEX* FUV, 1.5 arcsec). (f) H I (THINGS, 1.5 arcsec).
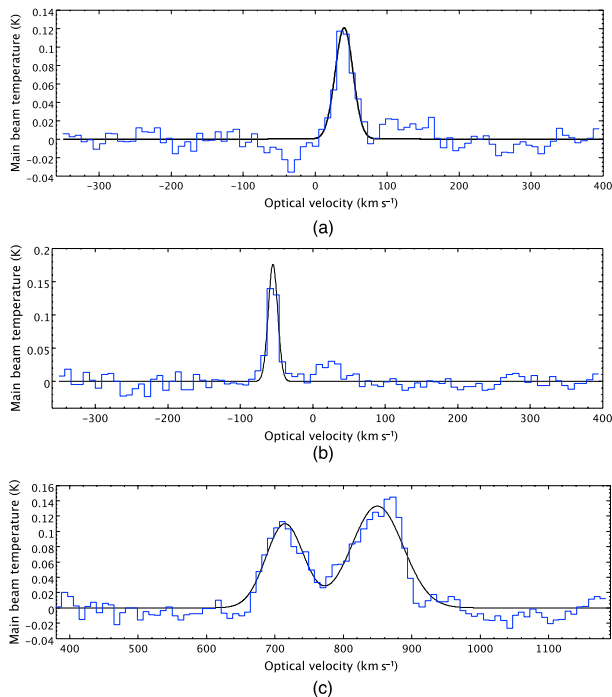
Figure 3. ^{12}CO $J = 3\rightarrow2$ spectra, on the main-beam antenna temperature (T_{mb}) scale, of the brightest pixels in NGC 2976 and NGC 3351, smoothed to $10\,\mathrm{km\,s^{-1}}$. All spectra are overlaid with Gaussian fits. The central velocity of spectrum (a) is fitted at $40.3\,\mathrm{km\,s^{-1}}$, with a peak temperature of $0.12\,\mathrm{K}$ and FWHM of $30.0\,\mathrm{km\,s^{-1}}$. Spectrum (b) has a central velocity of $-51.8\,\mathrm{km\,s^{-1}}$, with a peak temperature of $0.14\,\mathrm{K}$ and FWHM of $15.0\,\mathrm{km\,s^{-1}}$. Spectrum (c) has peak temperatures of 0.12 and $0.14\,\mathrm{K}$, with the lower peak velocity at $715\,\mathrm{km\,s^{-1}}$ and higher peak velocity at $850\,\mathrm{km\,s^{-1}}$. The FWHM is $72.4\,\mathrm{km\,s^{-1}}$ for the lower peak and $94.6\,\mathrm{km\,s^{-1}}$ for the higher peak. (a) North-west bright end region of NGC 2976 at RA 9:47:08.1 Dec +67:55:50.2 with $\sigma = 0.012\,\mathrm{K}$. (b) South-east bright end of NGC 2976 at RA 9:47:23.6 Dec +67:54:01.2 with $\sigma = 0.013\,\mathrm{K}$. (c) Central bright region of NGC 3351 at RA 10:43:57.6 Dec +11:42:13.9 with $\sigma = 0.012\,\mathrm{K}$.

and the inflow/outflow of gas within the inner bar. Each peak has a rather broad, $\sim$70–90 $\mathrm{km\,s^{-1}}$ half-power line width, with a peak intensity of $0.13\,\mathrm{K}$.

4.1 R_{31} line ratio and molecular gas mass

To estimate the H_2 molecular gas mass using the CO-to-H_2 conversion factor (X_{CO}), one often uses the ^{12}CO $J = 1\rightarrow0$ transition. However, as Greve et al. (2005) point out, the ^{12}CO $J = 1\rightarrow0$ line, which includes emission from the more diffuse molecular gas, does not trace star formation on a one-to-one basis. The ^{12}CO $J = 3\rightarrow2$ emission instead correlates almost linearly with the global SFR over five orders of magnitude (e.g. Iono et al. 2009). Hence, to derive M_{H_2} from the warmer and denser gas region, where ^{12}CO $J = 3\rightarrow2$ is thermalized, the ratio between ^{12}CO $J = 3\rightarrow2$ and ^{12}CO $J = 1\rightarrow0$ is important. For this purpose, we use the R_{31} map produced using the steps outlined in Section 3.1.1.

In Fig. 4(a), we plot the distribution of R_{31} across the disc of NGC 3351. Averaging R_{31} across the entire galaxy disc, we obtain a global mean ratio of 0.49 ± 0.03. This value agrees within $\sim$20 per cent with the R_{31} value obtained by comparing our map with the single-beam ^{12}CO $J = 1\rightarrow0$ observations, which are obtained from a central pointing on the galaxy. For example, using

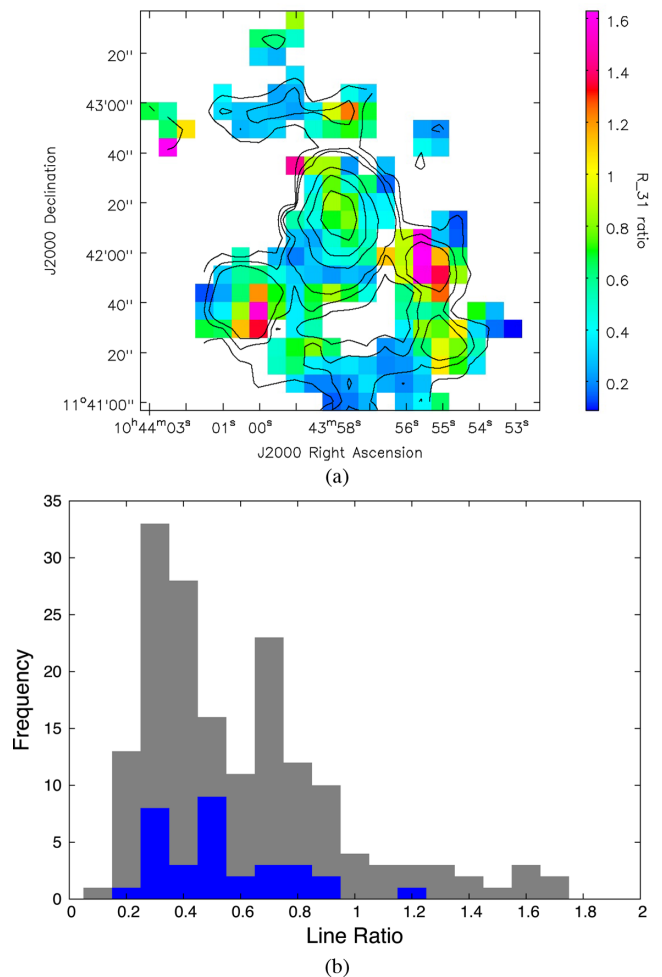**Figure 4.** Panel (a) shows the R_{31} ratio map for NGC 3351 constructed using the ^{12}CO $J = 1\rightarrow0$ map from the NRO Atlas. The grey contour line represents the ^{12}CO $J = 3\rightarrow2$ contour map to show the position of the ratio map relative to the galaxy. Panel (b) shows the distribution of the value of R_{31} across the galaxy. The grey histogram shows the pixel count when including all the pixels within the ratio map, whereas in the blue histogram we discard pixels within the ratio map with signal-to-noise ratio (SNR) less than 2. (a) Ratio map. (b) R_{31} distribution.

the ^{12}CO $J = 1\rightarrow0$ data from Sage (1993), we compute a ratio of 0.48 ± 0.03 for NGC 3351. The higher R_{31} observed near the complex that extends towards the south-west of the centre of NGC 3351 is the direct consequence of the offset in the detection of ^{12}CO $J = 3\rightarrow2$ and ^{12}CO $J = 1\rightarrow0$, as explained in Section 4.

Fig. 4(b) shows the variation of the R_{31} ratio within NGC 3351. The observed range of R_{31} values, mostly between 0.3 and 0.8, is similar to the range of global values obtained for the 28 nearby galaxies studied by Mauersberger et al. (1999) (0.2–0.7), and also similar to the range (0.4–0.8) observed in individual giant molecular clouds (GMCs) in M33 (Thornley & Wilson 1994; Wilson, Walker & Thornley 1997). We note that similar variations in R_{31} have been seen in other galaxies reported so far from the NGLS (Wilson et al. 2009; Bendo et al. 2010; Warren et al. 2010; Irwin et al. 2011; Sánchez-Gallego et al. 2011).

In Fig. 5, we plot R_{31} as a function of $I_{CO(1-0)}$, $I_{CO(3-2)}$ and the SFR surface density. We see only very weak correlation between the $I_{CO(1-0)}$ line brightness and R_{31}, indicating a very weak correlation in the spatial distribution of the total molecular gas mass, as traced
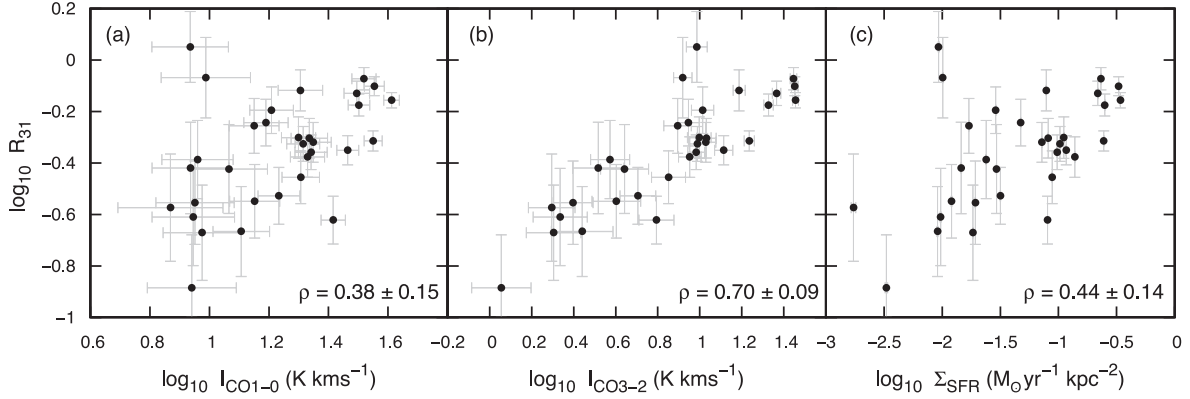
Figure 5. Correlation of R_{31} (with SNR > 2) with ^{12}CO $J = 1 \rightarrow 0$, ^{12}CO $J = 3 \rightarrow 2$ and SFR surface density, respectively, for NGC 3351. The Pearson correlation coefficient (ρ) is listed at the bottom left of each panel.

by $I_{CO(1-0)}$. We do, however, note a correlation between R_{31} and $I_{CO(3-2)}$, indicating that the $I_{CO(3-2)}$ line is bright where the line ratio is largest. This might also explain the very weak correlation between the R_{31} and the total molecular gas mass traced by $I_{CO(1-0)}$. The area with the bright ^{12}CO $J = 3 \rightarrow 2$ line indicates an area with denser gas, hence inevitably increasing the total molecular gas mass traced by $I_{CO(1-0)}$, as the less dense molecular gas is gravitationally attracted to the dense region. Plotting R_{31} against the SFR surface density maps in the rightmost panel of Fig. 5 reveals a weak correlation ($\rho = 0.44 \pm 0.14$). It appears that for NGC 3351, the warmer denser gas traced by high R_{31} ratios is reasonably well correlated with the star formation activity, on the spatial scales set by the pixel size of the map (108.9×10^3 pc^2).

We next derive M_{H_2} using the R_{31} value calculated from the ^{12}CO $J = 3 \rightarrow 2$ and the ^{12}CO $J = 1 \rightarrow 0$ data. The ^{12}CO luminosity is computed using the following expression:

$$L_{CO} = I_{avg} \times N_{pix} \times 23.5 \times (D \times \Delta_{pix})^2, \quad (3)$$

where L_{CO} is the ^{12}CO luminosity in K km s^{-1} pc^2, I_{avg} is the average ^{12}CO intensity (K km s^{-1}) obtained from the integrated intensity map on main-beam temperature scale, N_{pix} is the number of pixels included, D is the distance to the galaxy in Mpc and Δ_{pix} is the pixel size in arcseconds. The molecular gas mass is computed using

$$M_{H_2} = 1.6 \times 10^{-20} \times L_{CO} \times X_{CO}, \quad (4)$$

where $L_{CO} = L_{CO(3 \rightarrow 2)}/R_{31}$. In this paper, we use $X_{CO} = 2 \times 10^{20}$ (K km s^{-1})$^{-1}$ (Strong et al. 1988), consistent with other papers published in the NGLS series, and assume that this conversion factor does not vary across the galactic disc. We do not take into account the effects of metallicity. We note, however, that using the equation reported in Israel (2000) to calibrate X_{CO} for metallicity, the H$_2$ gas mass estimates for NGC 3351 would remain almost unchanged.

We now investigate the effect of various R_{31} values on M_{H_2}. First, we assume a generic line ratio of 0.6, which is a typical ratio appropriate for the molecular gas in Galactic and extragalactic GMCs (Wilson et al. 2009). Israel (2008) also found similar line ratios (0.6 ± 0.13) from observations of 15 nearby galaxies with modest starbursts. Secondly, we use the global mean ratio of 0.49 for NGC 3351, calculated directly from the present observations. The M_{H_2} derived using the global mean R_{31} value (0.49 ± 0.03) averaged across the disc of NGC 3351 is (3.3 ± 0.4) × 10^8 M$_\odot$ and agrees well (within the errors) with the value estimated using $R_{31} = 0.6$ from Wilson et al. (2009), which results in

$M_{H_2} = (2.7 \pm 0.3) \times 10^8$ M$_\odot$. Likewise for NGC 2976, using the Wilson et al. (2009) value, we compute M_{H_2} to be (0.27 ± 0.04) × 10^8 M$_\odot$ (we have not derived the R_{31} value for NGC 2976 due to the lack of calibrated ^{12}CO $J = 1 \rightarrow 0$ data from BIMA as explained previously). These estimates for the warmer gas (based on ^{12}CO $J = 3 \rightarrow 2$ data) are typically lower by a factor of 2–3 than the M_{H_2} based on lower-J ^{12}CO data [e.g. $M_{H_2} = 8.14 \times 10^8$ M$_\odot$ for NGC 3351 and $M_{H_2} = 0.61 \times 10^8$ M$_\odot$ as reported by Leroy et al. (2009) using their ^{12}CO $J = 2 \rightarrow 1$ HERACLES data] which traces more diffuse and cooler gas. We thus conclude that our estimates of the warm and denser gas (based on ^{12}CO $J = 3 \rightarrow 2$ data) are fairly insensitive against various R_{31} values.

4.1.1 Molecular gas mass and Σ_{SFR}

In this section, we investigate how the ratio H$_2$/H$\,$I (which we denote as R_{mol}) varies as a function of the Σ_{SFR} in two different environments, an H$\,$I-rich dwarf (NGC 2976) and an H$_2$-dominated galaxy (NGC 3351). We use the M_{H_2} values computed in Section 4.1 based on the generic $R_{31} = 0.6$ line ratio.

In Fig. 6, we plot the Σ_{SFR} as a function of the surface density of H$_2$ [Σ_{H_2} in panel 6(a)], surface density of total gas mass [$\Sigma_{H\,I + H_2}$ in panel 6(b)] and the ratio of H$_2$ to H$\,$I [R_{mol} in panel 6(c)]. In the case where ^{12}CO $J = 3 \rightarrow 2$ has been used to derive M_{H_2}, the data are shown as red circles and blue squares for NGC 3351 and NGC 2976, respectively. For comparison, we also show the distribution of M_{H_2} based on ^{12}CO $J = 1 \rightarrow 0$ which is applicable only in the case of NGC 3351 (yellow circles). Each point in these diagrams represents the corresponding quantity calculated within an area of 15.6×10^3 pc^2 for NGC 2976 and 108.9×10^3 pc^2 for NGC 3351 (which is the pixel size of our ^{12}CO $J = 3 \rightarrow 2$ maps). The surface densities of both molecular and atomic gas are calculated directly by dividing the gas mass estimated within that single pixel by the corresponding pixel area, taking into account the inclination of the galaxy. We find no correlation between the H$\,$I surface density ($\Sigma_{H\,I}$) and Σ_{SFR}; hence, we have not plotted it here, although we note that most pixels have $\Sigma_{H\,I}$ surface densities below 10 m$_\odot$ pc^{-2}, as seen in Schruba et al. (2011) and Leroy et al. (2008).

Fig. 6(a) shows that a tight correlation exists between Σ_{SFR} and H$_2$ surface density based on ^{12}CO $J = 3 \rightarrow 2$ data for NGC 3351 (power-law index $n = 1.53$). A similar trend is seen in Fig. 6(b) where Σ_{SFR} is plotted as a function of $\Sigma_{H\,I + H_2}$ ($n = 1.65$). However, when ^{12}CO $J = 1 \rightarrow 0$ data are used (yellow circles), then the slope of the correlation becomes steeper ($n = 2.46$ for Σ_{H_2} and $n = 2.75$
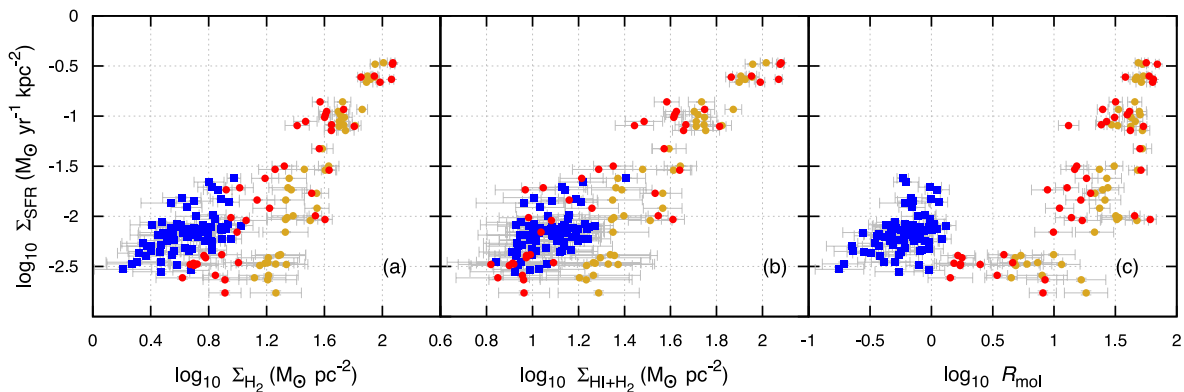
Figure 6. SFR density as a function of different gas phases: (left) H_2 only, (centre) $H_I + H_2$ and (right) H_2-to-H_I ratio. Each point in these diagrams represents a single pixel corresponding to the pixel size of our $^{12}CO\ J = 3 \rightarrow 2$ map. Pixels from NGC 2976 are plotted as blue squares, while regions from NGC 3351 are represented by red circles. The H_2 gas mass for both of these data sets was derived from our $^{12}CO\ J = 3 \rightarrow 2$ data, whereas the yellow diamond points represent the pixels from NGC 3351 in which the H_2 gas mass was derived from the NRO $^{12}CO\ J = 1 \rightarrow 0$ data.

for $\Sigma_{H_I + H_2}$, respectively). We suggest that the difference in slopes might be due to the fact that the diffuse areas where $^{12}CO\ J = 1 \rightarrow 0$ originates may not be directly related to active star formation.

In Fig. 6(c), we plot Σ_{SFR} as a function of R_{mol}. This plot clearly shows that NGC 2976 is mainly H_I dominated, whereas NGC 3351 is H_2 dominated. The pixel distribution for NGC 3351 shows a trend where higher R_{mol} values correspond to higher values of Σ_{SFR}. We suggest that this indicates that active star formation takes place in these areas (since there is more available H_2 to fuel star formation). No such trend is seen in NGC 2976. The power-law relation between R_{mol} and Σ_{SFR} is not surprising given the Schmidt–Kennicutt relation (Kennicutt 1989) that links areas of high H_2 concentration with higher rates of star formation (this relation is also reflected in Fig. 6a). Nevertheless, one would expect that the higher the H_2-to-H_I ratio, the higher is the rate of star formation (i.e. a tight power-law relation) if H_I does not contribute to star formation activity. But we do not see very distinctive evidence here. This might be due to the narrow dynamic range to fully sample the R_{mol} parameter space, or it could potentially show that the role of H_I in star formation cannot be completely ignored (Fumagalli & Gavazzi 2008; Leroy et al. 2008; Fumagalli et al. 2009; Glover & Clark 2012). In fact, as shown in Fig. 7(a), higher values of R_{mol} do indeed correlate with higher star formation efficiency SFE(H_I) (SFR surface density per unit H_I gas surface density), especially for NGC 3351.

However, this linear relationship between SFE(H_I) and R_{mol} is not seen with the SFE(H_2) (which is defined as the SFR surface density per unit H_2 gas surface density), nor with SFE($H_I + H_2$) (defined as the SFR surface density per unit neutral gas surface density), as shown in Figs 7(b) and (c). A further investigation collecting all the SINGS galaxies in the NGLS would be very instructive in this case.

4.2 Correlation with PAH emission

In both Figs 1 and 2, the large structures traced by $^{12}CO\ J = 3 \rightarrow 2$ appear to match those seen in the PAH 8 μm image. The two bright end regions of NGC 2976 can be seen in both wavebands. The ratio between the surface brightness of these bright end regions and that at the centre of the galaxy is larger in the PAH 8 μm image, and the weak inverse-S-shape structure that was visible in the $^{12}CO\ J = 3 \rightarrow 2$ map appears to show regions of stronger emission in the PAH 8 μm map as well. There is, however, a difference in the small-scale structures among these images. One example is the small structure directly to the south of the northern bright end region in the $^{12}CO\ J = 3 \rightarrow 2$ map (see contour at RA 09:47:10 and Dec. +67:55:30 of Fig. 1) which does not have a comparable counterpart in the PAH 8 μm image.

The emission from the central circumnuclear ring region of NGC 3351 dominates the brightness map in all three wavebands. The 2 arcmin ring structure is clearly seen in the PAH 8 μm image. This
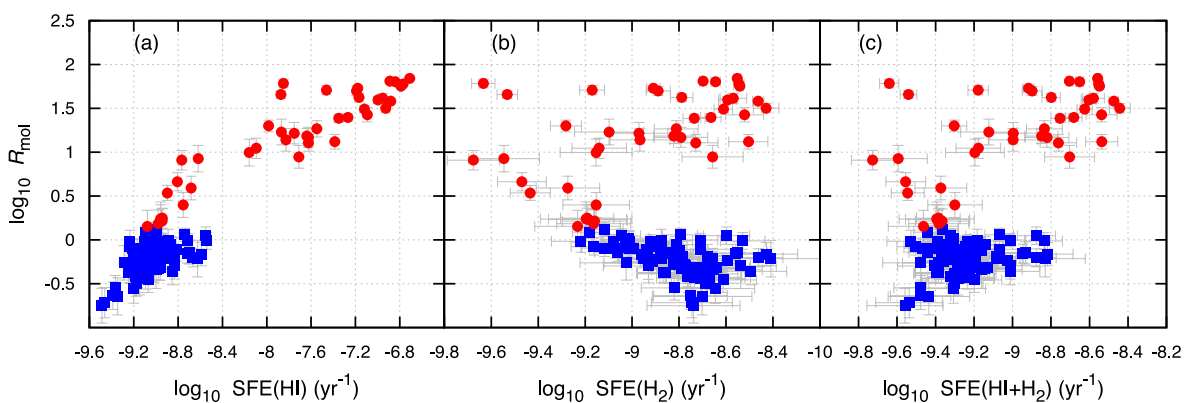

Figure 7. R_{mol} as a function of different star formation efficiencies: (left) SFE(H_I), (centre) SFE(H_2) and (right) SFE($H_I + H_2$). Each point in these diagrams represents a single pixel corresponding to the pixel size of our $^{12}CO\ J=3 \rightarrow 2$ map. Pixels from NGC 2976 are plotted as blue squares, while regions from NGC 3351 are represented by red circles.
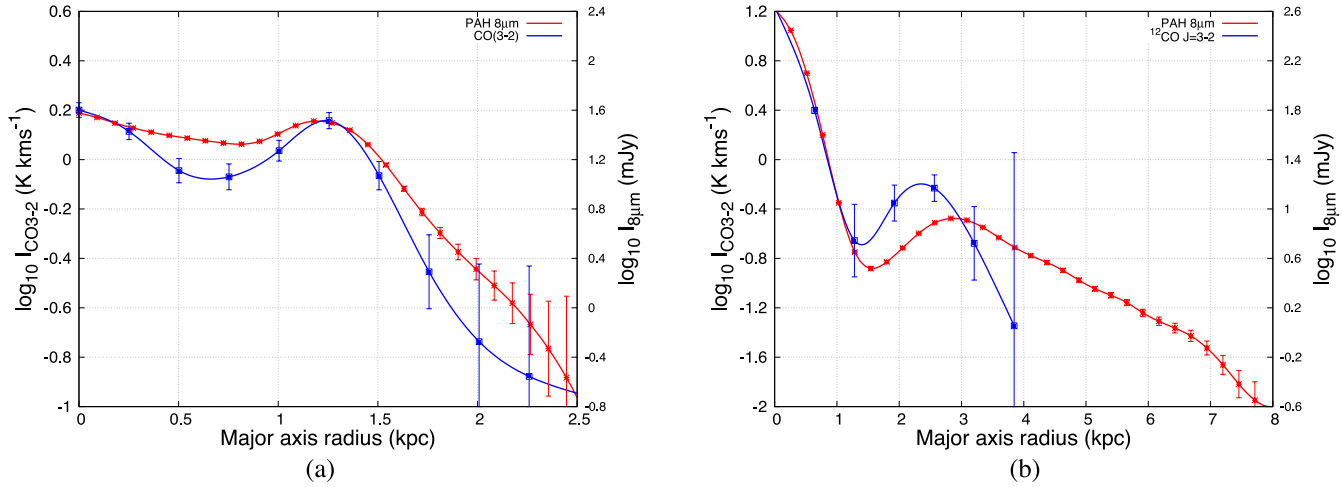
Figure 8. Comparison of the $^{12}CO\ J = 3 \rightarrow 2$ radial profile with that of *Spitzer* IRAC 8 μm for both NGC 2976 and NGC 3351. $^{12}CO\ J = 3 \rightarrow 2$ intensity is in K km s^{-1} (blue, left axis) and PAH 8 μm is in mJy (red, right axis). All data were convolved with kernels that match the PSF of $^{12}CO\ J = 3 \rightarrow 2$ data. (a) NGC 2976. (b) NGC 3351.

ring structure is only partially detected in the $^{12}CO\ J = 3 \rightarrow 2$ map. We note that the areas that were detected here do not seem any brighter in the PAH 8 μm image.

One might expect that $^{12}CO\ J = 3 \rightarrow 2$, which is excited in the warm and dense molecular gas regions nearer to the star formation sites, would have a high spatial correlation with PAH emission, if the PAH emission is connected to star formation activity. Regan et al. (2006) studied the radial distribution of the 8 μm emission and the $^{12}CO\ J = 1 \rightarrow 0$ emission for 11 disc galaxies and found a high spatial correlation between them. Bendo et al. (2010) compared the radial profiles of PAH 8 μm surface brightness to the $^{12}CO\ J = 3 \rightarrow 2$ in NGC 2403 and found that the scalelengths in both cases are statistically identical. But their examination in sub-kpc-scale regions within the galaxy revealed that $^{12}CO\ J = 3 \rightarrow 2$ and PAH 8 μm surface brightness seem to be uncorrelated. Here we further investigate this correlation for NGC 2976 and NGC 3351 by comparing the radial profiles of the $^{12}CO\ J = 3 \rightarrow 2$ emission to the PAH 8 μm surface brightness.

Fig. 8 shows the radial profile of PAH 8 μm and the $^{12}CO\ J = 3 \rightarrow 2$ surface brightness for both NGC 2976 and NGC 3351. The general shapes appear to match in both galaxies; however, on smaller spatial scales the agreement is less apparent.

The scalelengths, defined as the radial distances where the intensity drops by $1/e$ from the peak intensity, for NGC 2976 are 1.65 and 1.85 kpc for the $^{12}CO\ J = 3 \rightarrow 2$ and PAH 8 μm emission, respectively. These scalelengths are larger than the two bright end regions which correspond to the local maxima at $\sim$1.3 kpc away from the centre of the galaxy. Beyond $\sim$1.3 kpc, both emissions decay rapidly with almost the same rate. The ratio between the peak brightness of the two bright end regions and that at the galaxy centre, and the position of these bright end regions, is similar in both radial profiles. This might suggest that within high surface brightness regions, both components correlate better compared to lower brightness regions. Bendo et al. (2010) examined this relation in NGC 2403 at the sub-kpc scale and found a similar trend. In their plot,[11] it appears that both indicators only overlapped in the area

where the $^{12}CO\ J = 3 \rightarrow 2$ intensity is higher than 1.0 K km s^{-1} and PAH 8 μm surface brightness is higher than 2.0 MJy sr^{-1}.

Within the central $\sim$1 kpc of NGC 3351, the two radial profiles follow each other closely; this is likely to be due to the resolution limit imposed by the HARP-B beam size (FWHM of $\sim$660 pc at a distance of 9.33 mpc). The PSFs for both data have been convolved to the same resolution and the galaxy centre contains a bright source that is unresolved at the resolution of 14.5 arcsec. Away from the central region, the two profiles do not trace each other well anymore. Note that the ratio of the 2 arcmin ring-to-nucleus intensity of the $^{12}CO\ J = 3 \rightarrow 2$ is higher than the PAH 8 μm profile. Outside the 2 arcmin ring, the $^{12}CO\ J = 3 \rightarrow 2$ emission decays much faster than the PAH 8 μm emission, the latter extending almost twice as far as the $^{12}CO\ J = 3 \rightarrow 2$ profile. As we saw in NGC 2976, this might indicate that the correlation of the two components is better in a higher brightness region in the galaxy. But again, the detection of $^{12}CO\ J = 3 \rightarrow 2$ in this region is too faint to reach a definite conclusion.

To further examine this relation, we compare both detections pixel by pixel and plot their correlation in Fig. 9, using only the pixels detected within our $^{12}CO\ J = 3 \rightarrow 2$ map. Again, the PAH 8 μm map is convolved and re-gridded to match the resolution of our $^{12}CO\ J = 3 \rightarrow 2$ map. Note that due to the difference in distance, each point within this plot corresponds to an area of 15.6×10^3 pc^2 for NGC 2976 and 108.9×10^3 pc^2 for NGC 3351. As with the radial profile comparison, this pixel-by-pixel approach seems to show that both kinds of emission are quite well correlated globally. However, there seems to be a larger scatter at the higher surface brightness end of the plot, and the correlation seems to break down at $\log L_{CO3 \rightarrow 2} < 4.5$. This seems to agree with the argument from Bendo et al. (2010) that this correlation would break down at lower intensity or smaller spatial scales. It would be interesting to further examine this relation with a larger sample of galaxies to determine where this correlation begins to fail.

In order to determine whether this relationship only holds for these two galaxies, we examined all the SINGS galaxies within the NGLS to see if NGC 2976 and NGC 3351 are typical of the entire sample. The other field and Virgo galaxies within the NGLS samples were not included here, as they lack the corresponding PAH 8 μm data from the SINGS. In Fig. 10, we plot the *total* $^{12}CO\ J = 3 \rightarrow 2$
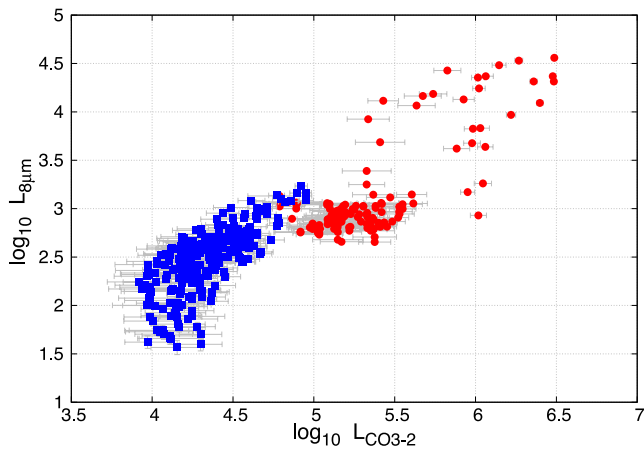
[11] Fig. 14 in Bendo et al. (2010).

Figure 9. Pixel-by-pixel comparison of the ^{12}CO $J = 3→2$ luminosity with the PAH 8 μm luminosity. Each red circle represents a pixel from NGC 3351, while each blue square corresponds to a single pixel in the NGC 2976 map.
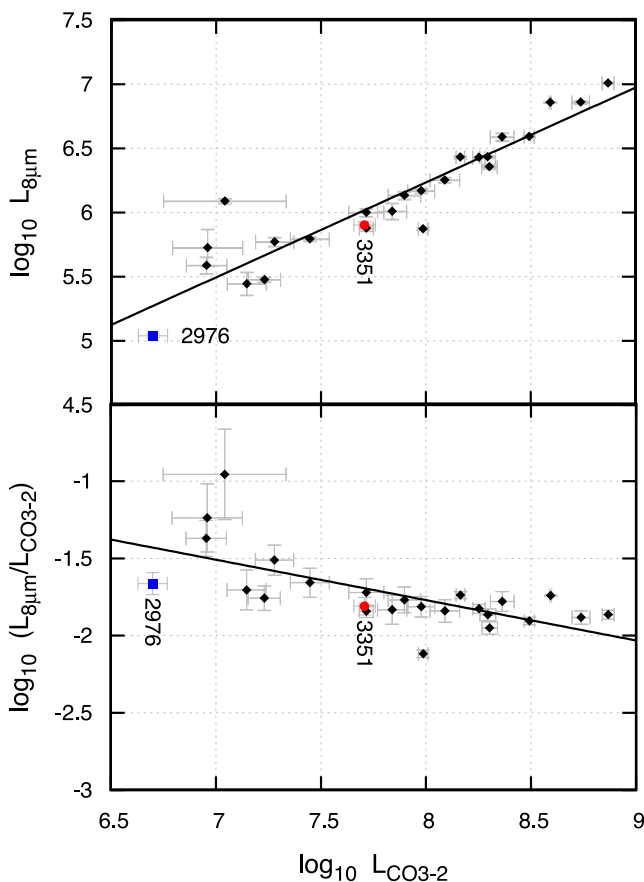

Figure 10. Correlation of the total integrated PAH 8 μm luminosity and the total integrated ^{12}CO $J = 3→2$ luminosity of the 25 SINGS galaxies in the NGLS samples.

luminosity against the *total* PAH 8 μm luminosity for NGC 2976 and NGC 3351, together with 23 SINGS galaxies that have ^{12}CO $J = 3→2$ detected. The luminosity values are tabulated in Table 3. The ^{12}CO $J = 3→2$ maps of these 23 galaxies are obtained from the early release of the NGLS data set (Wilson et al. 2012). The PAH 8 μm maps are obtained from the same source as described in Section 2.1.

Table 3. *Total* luminosity of PAH 8 μm and ^{12}CO $J = 3→2$ of 25 SINGS galaxies within the NGLS samples.

Galaxy	Distance (Mpc)	$L_{PAH\,8\,μm}$ (MJy pc^2)	$L_{CO(3–2)}$ ($×10^7$ K km s^{-1} pc^2)
NGC 0628	7.3	0.99 ± 0.07	5.2 ± 1.0
NGC 0925	9.1	0.38 ± 0.15	0.9 ± 0.2
NGC 2403	3.2	0.30 ± 0.04	1.7 ± 0.3
NGC 2841	14.1	1.22 ± 0.04	< 1.1
NGC 2976	3.6	0.11 ± 0.03	0.50 ± 0.08
NGC 3031	3.6	0.53 ± 0.33	0.91 ± 0.35
NGC 3034	3.6	7.12 ± 0.01	39.2 ± 0.4
NGC 3049	22.7	0.26 ± 0.21	1.4 ± 0.3
NGC 3184	11.1	1.46 ± 0.04	9.5 ± 1.4
NGC 3198	13.7	1.01 ± 0.14	6.9 ± 1.1
NGC 3351	9.3	0.79 ± 0.06	5.1 ± 0.6
NGC 3521	7.9	2.53 ± 0.01	17.9 ± 1.2
NGC 3627	9.4	3.86 ± 0.01	31.1 ± 1.7
NGC 3938	14.7	1.65 ± 0.05	12.3 ± 2.0
NGC 4254	16.7	10.06 ± 0.02	73.8 ± 4.8
NGC 4321	16.7	7.14 ± 0.02	54.7 ± 5.3
NGC 4559	9.3	0.58 ± 0.08	1.9 ± 0.4
NGC 4569	16.7	2.25 ± 0.04	20.1 ± 1.7
NGC 4579	16.7	1.34 ± 0.07	7.9 ± 1.4
NGC 4631	7.7	2.67 ± 0.02	14.6 ± 0.7
NGC 4736	5.2	0.75 ± 0.05	5.2 ± 0.4
NGC 4826	7.5	0.74 ± 0.02	9.7 ± 0.5
NGC 5033	16.2	3.60 ± 0.07	23.1 ± 3.0
NGC 5055	7.9	2.75 ± 0.02	19.7 ± 1.7
UGC 05720	25.0	0.58 ± 0.04	2.8 ± 0.6

Clearly, the correlation of the two indicators is tight. There seems to be an approximately linear relation between the two, with $\log L_{8\,μm} ≈ (0.74 ± 0.06) \log I_{CO(3–2)} - 0.32$. The Pearson correlation coefficient is as high as 0.97, with both NGC 2976 and NGC 3351 lying close to the best-fitting line. To investigate whether this tight relation is not entirely dominated by the strong nuclear emission regions, we made a similar plot of the median luminosity instead of the total luminosity and found that the high correlation still holds.

Even though both ^{12}CO $J = 3→2$ and PAH 8 μm are believed to be linked to star formation, their origins within the ISM and their fundamental excitation mechanisms are different (e.g. Young & Scoville 1991; Tielens 2008). The 8 μm emission originates from PAHs found near the stars, in particular in the photospheres of asymptotic giant branch stars (Tielens 2008), while molecular CO is formed on the surface of interstellar dust grains. The surface brightness of PAH 8 μm emission is mostly proportional to the number of FUV photons and the number density of PAH molecules. The ^{12}CO $J = 3→2$ intensity, on the other hand, is controlled mainly by the collision rate with the molecular hydrogen, the temperature of the gas and the density of molecular hydrogen. It is thus important to understand why they correlate so well in a global environment.

One possible explanation is that there is a spatial coexistence of the PAH molecules and molecular CO in photodissociation regions (PDR), although not at specific sub-kpc locations within individual clouds. At the front of a PDR, the UV flux from hot stars or the interstellar radiation field excites the PAH molecules and heats the small grains in the ISM. This is responsible for the generation of intense radiation from PAHs and the continuum dust emission in the mid-infrared. CO rotational transitions are generally believed to be generated from regions that reside deeper in the PDR (Hollenbach &

Tielens 1999). In this region, the UV source is still strongly photodissociating species like OH and H_2O, but is weaker compared to the ionization front, and thus molecular hydrogen and CO start to form in this region. Given a certain amount of UV photons, a higher density of PAHs would absorb a larger portion of these stellar fluxes, and reduce the photodissociation of CO molecules, hence resulting in a positive correlation of the two constituents. Also, both PAHs and molecular CO would not exist in high UV radiation region, as both species would be dissociated.

The same scenario can be applied to the star-forming regions within the molecular clouds. If the $^{12}CO\ J = 3 \rightarrow 2$ intensity indicates the amount of gas fuelling star formation in the core, it could be approximately proportional to the number of UV photons radiated by these newly born O and B stars. If a linear fraction of these photons is absorbed by the PAHs, their surface brightness will then be approximately proportional to the $^{12}CO\ J = 3 \rightarrow 2$ intensity.

There are other alternative explanations in the literature, for example the association between the PAH emission and the cold dust (Haas et al. 2002; Bendo et al. 2008). If molecular gas is associated with cold dust, then the PAH and $^{12}CO\ J = 3 \rightarrow 2$ would be expected to be associated with each other as well. In general, we find that the $^{12}CO\ J = 3 \rightarrow 2$ luminosity does correlate well with PAH 8 μm luminosity at large scales, but this correlation might not hold for smaller sub-kpc scale.

5 SUMMARY AND CONCLUSIONS

We have presented the $^{12}CO\ J = 3 \rightarrow 2$ maps of NGC 2976 and NGC 3351, obtained using HARP-B on the JCMT. We compared our observations to the optical, $^{12}CO\ J = 1 \rightarrow 0$, PAH 8 μm, H I and Σ_{SFR} maps constructed using a combination of 24 μm and FUV data. $^{12}CO\ J = 3 \rightarrow 2$ emission from NGC 2976 was strong at both ends of the galaxy's major axis, whereas in NGC 3351 the emission peaks in the nuclear region. NGC 2976 showed a large-scale structure that was seen only in the $^{12}CO\ J = 2 \rightarrow 1$ image, but not in other wavebands included in this paper, due to the coarse resolution of the $^{12}CO\ J = 3 \rightarrow 2$ and $^{12}CO\ J = 1 \rightarrow 0$ maps. In contrast, the dominant circumnuclear region in NGC 3351 was visible in all waveband maps presented here. However, the prominent 2 arcmin ring structure was only weakly detected in our $^{12}CO\ J = 3 \rightarrow 2$ map.

We combined our $^{12}CO\ J = 3 \rightarrow 2$ data with $^{12}CO\ J = 1 \rightarrow 0$ data from various sources to derive the R_{31} line ratio (for NGC 3351). The ratio values we obtained were within the ranges derived from various nearby galaxy surveys. We then computed M_{H_2} using the derived R_{31} as well as the generic value 0.6 from Wilson et al. (2009). We found that M_{H_2} estimates are robust against the value of R_{31} used.

We further examined the correlation between Σ_{SFR} and surface density of H_2 mass and neutral hydrogen gas mass. We found that the Σ_{SFR} correlates better with the $^{12}CO\ J = 3 \rightarrow 2$ emission. We used the H I data from THINGS to derive the H_2-to-H I ratio and compared it with the SFE(H I). We found that although NGC 2976 is H I dominated and NGC 3351 is an H_2-dominated galaxy, they both show a correlation between R_{mol} and SFE(H I), which implies that the role of H I in star formation cannot be excluded.

We have also studied the correlation between the $^{12}CO\ J = 3 \rightarrow 2$ and PAH 8 μm surface brightness as both are prominent indicators linked to star formation activity. We first investigated their relation within NGC 2976 and NGC 3351 using both the radial distribution of the surface brightness and a pixel-by-pixel comparison. We found that they correlate well in the higher surface brightness regions. We

further studied the global correlation between the *total* luminosities of the two physical parameters using the data from all 25 SINGS galaxies within the NGLS and reached a similar conclusion. We suggest that this could be the result of the coexistence of both ^{12}CO and PAH molecules in the PDR regions, provided that the lifetimes of both species are matched. In conclusion, we suggest that this correlation is high at large spatial scales, but at smaller sub-kpc scales, the correlation may break down.

REFERENCES

Abazajian K. N. et al., 2009, ApJS, 182, 543
Albrecht M., Chini R., Krügel E., Müller S. A. H., Lemke R., 2004, A&A, 414, 141
Alloin D., Nieto J.-L., 1982, A&AS, 50, 491
Appleton P. N., Davies R. D., Stephenson R. J., 1981, MNRAS, 195, 327
Bendo G. J. et al., 2006, ApJ, 652, 283
Bendo G. J. et al., 2008, MNRAS, 389, 629
Bendo G. J. et al., 2010, MNRAS, 402, 1409
Braine J., Combes F., Casoli F., Dupraz C., Gerin M., Klein U., Wielebinski R., Brouillet N., 1993, A&AS, 97, 887
Buckle J. V. et al., 2009, MNRAS, 399, 1026
Buta R., Crocker D. A., 1993, AJ, 105, 1344
Buta R. J., Corwin H. G., Odewahn S. C., 2007, The de Vaucouleurs Altlas of Galaxies. Cambridge Univ. Press, Cambridge
Calzetti D., 2012, in Falcon-Barroso J., Knapen J. H., eds, Proc. of the XXIII Canary Islands Winter School of Astrophysics: Secular Evolution of Galaxies, Star Formation Rate Indicators. Cambridge Univ. Press, Cambridge, in press (arXiv:1208.2997)
Calzetti D. et al., 2005, ApJ, 633, 871
Calzetti D. et al., 2007, ApJ, 666, 870
Colina L., Garcia Vargas M. L., Mas-Hesse J. M., Alberdi A., Krabbe A., 1997, ApJ, 484, L41
Comerón S., Knapen J. H., Beckman J. E., Laurikainen E., Salo H., Martínez-Valpuesta I., Buta R. J., 2010, MNRAS, 402, 2462
Comerón S. et al., 2013, A&A, submitted

Dale D. A. et al., 2009, ApJ, 703, 517

de Blok W. J. G., Walter F., Brinks E., Trachternach C., Oh S., Kennicutt R. C., 2008, AJ, 136, 2648

de Vaucouleurs G., de Vaucouleurs A., Corwin H. G., Buta R. J., Paturel G., Fouque P., 1995, VizieR Online Data Catalog, 7155

Elfhag T., Booth R. S., Hoeglund B., Johansson L. E. B., Sandqvist A., 1996, A&AS, 115, 439

Elmegreen D. M., Chromey F. R., Santos M., Marshall D., 1997, AJ, 114, 1850

Freedman W. L. et al., 2001, ApJ, 553, 47

Frei Z., Guhathakurta P., Gunn J. E., Tyson J. A., 1996, AJ, 111, 174

Fumagalli M., Gavazzi G., 2008, A&A, 490, 571

Fumagalli M., Krumholz M. R., Prochaska J. X., Gavazzi G., Boselli A., 2009, ApJ, 697, 1811

Glover S. C. O., Clark P. C., 2012, MNRAS, 421, 9

Gordon K. D., Engelbracht C. W., Rieke G. H., Misselt K. A., Smith J.-D. T., Kennicutt R. C., Jr, 2008, ApJ, 682, 336

Greve T. R. et al., 2005, MNRAS, 359, 1165

Haas M., Klaas U., Bianchi S., 2002, A&A, 385, L23

Hägele G. F., Díaz Á. I., Cardaci M. V., Terlevich E., Terlevich R., 2007, MNRAS, 378, 163

Helfer T. T., Thornley M. D., Regan M. W., Wong T., Sheth K., Vogel S. N., Blitz L., Bock D. C.-J., 2003, ApJS, 145, 259

Helou G. et al., 2004, ApJS, 154, 253

Hollenbach D. J., Tielens A. G. G. M., 1999, Rev. Mod. Phys., 71, 173

Iono D. et al., 2009, ApJ, 695, 1537

Irwin J. A. et al., 2011, MNRAS, 410, 1423

Israel F., 2000, in Combes F., Pineau Des Forets G., eds, Molecular Hydrogen in Space. Cambridge Univ. Press, Cambridge, p. 293

Israel F. P., 2005, A&A, 438, 855

Israel F. P., 2008, in Kramer C., Aalto S., Simon R., eds, EAS Publ. Ser. Vol. 31, Molecular Gas in Spiral Galaxy Centers. Cambridge Univ. Press, Cambridge. p. 89

Jenness T., Berry D. S., Cavanagh B., Currie M. J., Draper P. W., Economou F., 2009, in Bohlender D. A., Durand D., Dowler P., eds, ASP Conf. Ser. Vol. 411, Developments in the Starlink Software Collection. Astron. Soc. Pac., San Francisco, p. 418

Karachentsev I. D. et al., 2002, A&A, 383, 125

Kennicutt R. C., Jr, 1989, ApJ, 344, 685

Kennicutt R. C., Jr et al., 2003, PASP, 115, 928

Kennicutt R. C. et al., 2009, ApJ, 703, 1672

Knapen J. H., Pérez-Ramírez D., Laine S., 2002, MNRAS, 337, 808

Krist J., 2002, Tiny Tim/SIRTF User's Guide, SSC, Pasadena

Kuno N. et al., 2007, PASJ, 59, 117

Laine S., 2011, IRAC Instrument Handbook, available at: http://irsa.ipac.caltech.edu/data/SPITZER/docs/irac/iracinstrumenthandbook/

Leroy A. K., Walter F., Brinks E., Bigiel F., de Blok W. J. G., Madore B., Thornley M. D., 2008, AJ, 136, 2782

Leroy A. K. et al., 2009, AJ, 137, 4670

Mauersberger R., Henkel C., Walsh W., Schulz A., 1999, A&A, 341, 256

Meier D. S., Turner J. L., Crosthwaite L. P., Beck S. C., 2001, AJ, 121, 740

Prescott M. K. M. et al., 2007, ApJ, 668, 182

Reach W. T. et al., 2005, PASP, 117, 978

Regan M. W., Thornley M. D., Helfer T. T., Sheth K., Wong T., Vogel S. N., Blitz L., Bock D. C.-J., 2001, ApJ, 561, 218

Regan M. W. et al., 2006, ApJ, 652, 1112

Sage L. J., 1993, A&AS, 100, 537

Sakamoto K., Okumura S. K., Ishizuki S., Scoville N. Z., 1999, ApJS, 124, 403

Sánchez-Gallego J. R. et al., 2011, A&A, 527, A16

Schruba A. et al., 2011, AJ, 142, 37

Simon J. D., Bolatto A. D., Leroy A., Blitz L., 2003, ApJ, 596, 957

Smith H. et al., 2003, in Phillips T. G., Zmuidzinas J., eds, Proc. SPIE Conf. Ser. Vol. 4855, HARP-B: A 350-GHz 16-element Focal Plane Array for the James Clerk Maxwell Telescope. SPIE, Bellingham, p. 338

Smith J. D. T. et al., 2007, ApJ, 656, 770

Strong A. W. et al., 1988, A&A, 207, 1

Swartz D. A., Yukita M., Tennant A. F., Soria R., Ghosh K. K., 2006, ApJ, 647, 1030

Thornley M. D., Wilson C. D., 1994, ApJ, 421, 458

Tielens A. G. G. M., 2008, ARA&A, 46, 289

Warren B. E. et al., 2010, ApJ, 714, 571

Williams B. F. et al., 2010, ApJ, 709, 135

Wilson C. D., Walker C. E., Thornley M. D., 1997, ApJ, 483, 210

Wilson C. D. et al., 2009, ApJ, 693, 1736

Wilson C. D. et al., 2012, MNRAS, 424, 3050

Young J. S., Scoville N. Z., 1991, ARA&A, 29, 581

Young J. S. et al., 1995, ApJS, 98, 219

Yun M. S., 1999, in Barnes J. E., Sanders D. B., eds, Proc. IAU Symp. 186, Galaxy Interactions at Low and High Redshift. Kluwer, Dordrecht, p. 81

Zhu Y.-N., Wu H., Cao C., Li H.-N., 2008, ApJ, 686, 155

This paper has been typeset from a TeX/LaTeX file prepared by the author.